

# Elastic $\alpha$ -scattering of $^{112}\text{Sn}$ and $^{124}\text{Sn}$ at astrophysically relevant energies

D. Galaviz,<sup>1,\*</sup> Zs. Fülöp,<sup>2</sup> Gy. Gyürky,<sup>2</sup> Z. Máté,<sup>2</sup> P. Mohr,<sup>1,†</sup> T. Rauscher,<sup>3</sup> E. Somorjai,<sup>2</sup> and A. Zilges<sup>1</sup>

<sup>1</sup> *Institut für Kernphysik, Technische Universität Darmstadt, Schlossgartenstraße 9, D-64289 Darmstadt, Germany*

<sup>2</sup> *ATOMKI, PO Box 51, H-4001 Debrecen, Hungary*

<sup>3</sup> *Departement für Physik und Astronomie, Universität Basel, Klingelbergstrasse 82, CH-4056 Basel, Switzerland*

(Dated: June 28, 2018)

## Abstract

The cross sections for the elastic scattering reactions  $^{112,124}\text{Sn}(\alpha,\alpha)^{112,124}\text{Sn}$  at energies above and below the Coulomb barrier are presented and compared to predictions for global  $\alpha$ -nucleus potentials. The high precision of the new data allows a study of the global  $\alpha$ -nucleus potentials at both the proton and neutron-rich sides of an isotopic chain. In addition, local  $\alpha$ -nucleus potentials have been extracted for both nuclei, and used to reproduce elastic scattering data at higher energies. Predictions from the capture cross section of the reaction  $^{112}\text{Sn}(\alpha,\gamma)^{116}\text{Te}$  at astrophysically relevant energies are presented and compared to experimental data.

PACS numbers: 24.10.Ht, 25.55.-e, 25.55.Ci, 26.30.+k

---

\*Electronic address: galaviz@nscl.msu.edu; Present address: NSCL, Michigan State University, 1 Cyclotron Lab, East Lansing, MI 48824-1321, USA

†Present address: Strahlentherapie, Diakoniekrankenhaus Schwäbisch Hall, D-74523 Schwäbisch Hall, Germany

## I. INTRODUCTION

The 35 most proton-rich, stable isotopes between Se and Hg are called  $p$  nuclei. Contrary to the synthesis of most nuclei above Fe through neutron captures in the  $s$  and  $r$  process [1], the production of the  $p$  nuclei proceeds mainly via photon-induced reactions at temperatures around a few GK [2, 3]. Seed nuclei already present in the stellar plasma and originating from the  $s$  and  $r$  process are disintegrated mainly by  $(\gamma, n)$ ,  $(\gamma, p)$  and  $(\gamma, \alpha)$  reactions in the thermal photon bath of the corresponding explosive astrophysical event. Due to persisting problems in the reproduction of the observed  $p$  abundances, a definite conclusion on the actual site of this nucleosynthesis process – usually called  $p$  or  $\gamma$  process – cannot be drawn yet, however, the commonly most favored site providing the required conditions is explosive Ne/O burning in type II supernovae [2, 4, 5]. Recently, consistent studies of  $p$  nucleosynthesis have become available, employing theoretical reaction rates in large reaction networks [4, 5, 6]. For heavy nuclei ( $140 \lesssim A \lesssim 200$ ),  $(\gamma, n)$  and  $(\gamma, \alpha)$  reactions play the dominant role while other photon-induced reactions are practically negligible. This is not the case for lighter nuclei where captures and photodisintegrations involving neutrons, protons, and  $\alpha$  particles have to be considered [7, 8]. Finally, neutrino-induced reactions may have some importance for selected isotopes because of the high neutrino-flux stemming from the core collapse triggering the type II supernova explosion [4, 5].

The cross sections used to calculate the required astrophysical reaction rates in network studies are based on the statistical model (Hauser-Feshbach) [9, 10, 11, 12, 13]. Global optical potentials are considered in these calculations encompassing many hundreds of nuclei and several thousand reactions. Experimental data is scarce due to the sub-Coulomb energies and the large number of unstable nuclei relevant for astrophysical applications. Only recently, a number of experiments has been devoted to the study of cross sections at astrophysically relevant energies. However, there is still a lack of relevant experimental data for  $(\gamma, \alpha)$  and  $(\alpha, \gamma)$  reactions because of the high Coulomb barriers. Recent  $\alpha$  capture experiments on heavy nuclei at astrophysically relevant energies were performed on  $^{70}\text{Ge}$  [14],  $^{96}\text{Ru}$  [15],  $^{112}\text{Sn}$  [16] and  $^{144}\text{Sm}$  [17]. No experimental data for  $(\gamma, \alpha)$  cross sections are available at astrophysically interesting energies.

In general,  $(\alpha, \gamma)$  and  $(\gamma, \alpha)$  reaction cross sections are very sensitive to the choice of the  $\alpha$ -nucleus potential, as has been observed in the huge uncertainties for the prediction of the

$^{144}\text{Sm}(\alpha,\gamma)^{148}\text{Gd}$  cross section [17, 18, 19]. Elastic  $\alpha$  scattering at low energies (close to the Coulomb barrier) should provide an additional test for the  $\alpha$ -nucleus potentials considered in  $p$  process network calculations. High precision data are needed for a clear determination of the optical potential properties at the measured energies.

In this work the cross sections for the reactions  $^{112,124}\text{Sn}(\alpha,\alpha)^{112,124}\text{Sn}$  at energies above and below the Coulomb barrier are presented. The new experimental data provide a test for the global parameterizations considered in  $p$  process network calculations. Furthermore, the study of both proton- and neutron-rich stable tin isotopes provides important information about the variation of  $\alpha$ -nucleus potentials along an isotopic chain. A local  $\alpha$ -nucleus potential is derived for both neutron-deficient ( $^{112}\text{Sn}$ ) and neutron-rich ( $^{124}\text{Sn}$ ) nuclei.

In this paper we first present the experimental procedure (Sec. II) and compare the results to existing global  $\alpha$ -nucleus potentials (Sec. III A). The determination of the potential for the tin isotopes is performed within the Optical Model (OM) framework (Sec. III B), and the results are compared to previous experimental data (Secs. III C–D). In addition, the derived potential for  $^{112}\text{Sn}$  is used for a prediction of the  $^{112}\text{Sn}(\alpha,\gamma)^{116}\text{Te}$  cross section which has been recently measured using the activation technique [16] (Sec. IV).

## II. EXPERIMENTAL PROCEDURE AND RESULTS

The scattering experiments were performed at the cyclotron laboratory of ATOMKI, Debrecen, Hungary, where  $^4\text{He}^{2+}$  beams are available up to energies of about  $E_\alpha = 20$  MeV. Angular distributions were measured for  $^{112}\text{Sn}$  at  $E_\alpha = 19.5$  MeV and 14.4 MeV, and for  $^{124}\text{Sn}$  at  $E_\alpha = 19.5$  MeV. The beam intensity was approximately 300 nA. The experimental setup was similar to the one used in our previous experiments on  $^{144}\text{Sm}$  [18] and  $^{92}\text{Mo}$  [20]. Further experimental details on the setup can be found in [21]. Here we briefly summarize the most important features of the setup.

The angular distributions were measured using four silicon surface-barrier detectors mounted on two turntables. The solid angles varied between  $1.55 \times 10^{-4}$  sr and  $1.63 \times 10^{-4}$  sr. Two additional detectors placed at  $15^\circ$  left and right to the incoming beam axis with solid angles of  $8.1 \times 10^{-6}$  sr are used to normalize the angular distributions and to determine the beam position on the target with high precision. Note that small horizontal deviations of about 1 mm lead to corrections of the cross section of the order of 1 % at very forward angles.

These corrections can be precisely determined from the ratio of the count rates in the two monitor detectors.

The targets consisted of highly enriched  $^{112}\text{Sn}$  (99.6%) and  $^{124}\text{Sn}$  (97.4%) deposited onto thin carbon backings. The target thicknesses of  $200\ \mu\text{g}/\text{cm}^2$  for both isotopes were confirmed by the measured Rutherford cross sections during the experiment. The absolute normalization was obtained from the Rutherford cross section at very forward angles [18, 20].

A precise dead time correction is necessary especially at forward angles where the cross sections are huge. Therefore, the dead time was monitored using pulse generators in all spectra. Typical spectra of the  $^{112}\text{Sn}(\alpha,\alpha)^{112}\text{Sn}$  and  $^{124}\text{Sn}(\alpha,\alpha)^{124}\text{Sn}$  reactions are shown in Fig. 1.

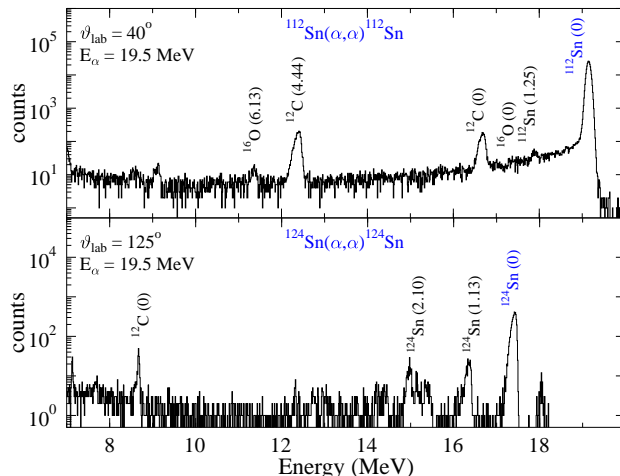


FIG. 1: Spectra of the  $^{112}\text{Sn}(\alpha,\alpha)^{112}\text{Sn}$  and  $^{124}\text{Sn}(\alpha,\alpha)^{124}\text{Sn}$  reactions at  $E_\alpha = 19.5\ \text{MeV}$  at forward ( $\vartheta_{\text{lab}} = 40^\circ$ ) and backward ( $\vartheta_{\text{lab}} = 125^\circ$ ) angles, respectively. Elastic scattering on target contaminations (mainly  $^{12}\text{C}$  from the carbon backing) and inelastically scattered events are clearly separated from the elastic peak. A small target contamination with  $A \approx 200$  which is visible only in the spectra at backward angles remains below 1% contribution to the elastic peaks. The pulser signals used for dead time correction are not seen in the spectra, as they lay above the shown energy region.

From a kinematic coincidence between the  $\alpha$  particles scattered on a  $20\ \mu\text{g}/\text{cm}^2$  carbon backing foil and the  $^{12}\text{C}$  recoil nuclei, we calibrated the position of the silicon detectors with a precision of  $\Delta\vartheta = 0.07^\circ$ . The scattered  $\alpha$  particles were measured using one detector

placed at  $\vartheta_{lab} = 70^\circ$  (right side relative to beam axis). The recoil  $^{12}\text{C}$  nuclei from the elastic ( $^{12}\text{C}_{gs}$ ) and inelastic ( $^{12}\text{C}_{2+}$ ,  $E_x=4.44$  MeV) scattering were measured with another detector (left side) which was moved around the expected positions,  $\vartheta_{lab,el.} = 45.83^\circ$  and  $\vartheta_{lab,inel.} = 38.89^\circ$ . The results are shown in Fig. 2. The maximum recoil rate is observed at the expected position within the statistical uncertainties.

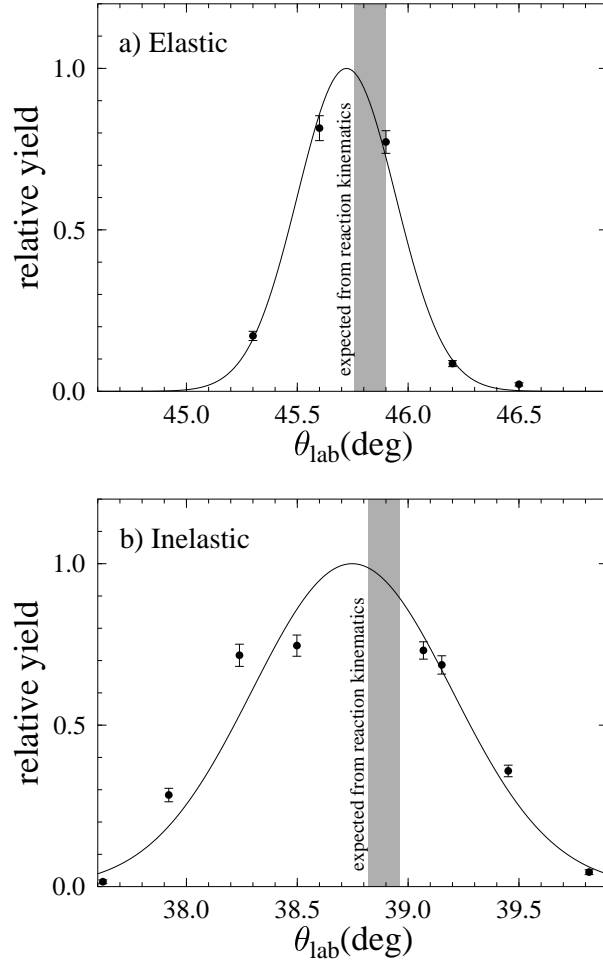


FIG. 2: Relative yield of  $^{12}\text{C}$  recoil nuclei in coincidence with a) elastically and b) inelastically scattered  $\alpha$  particles. A Gaussian fit to the experimental data (solid line) is shown to guide the eye. The shaded area presents the angle and the uncertainty expected from the measured reaction kinematics.

From the yield in the elastic peaks, the elastic scattering cross section is calculated. The data is normalized to the Rutherford cross section of point-like charged particles. The ex-

perimental results are shown in Fig. 3. Note that the measured cross sections cover more than four orders of magnitude in the whole angular range. Nevertheless, typical uncertainties remain below 3–4 % for all measured data points, including systematic and statistical uncertainties.

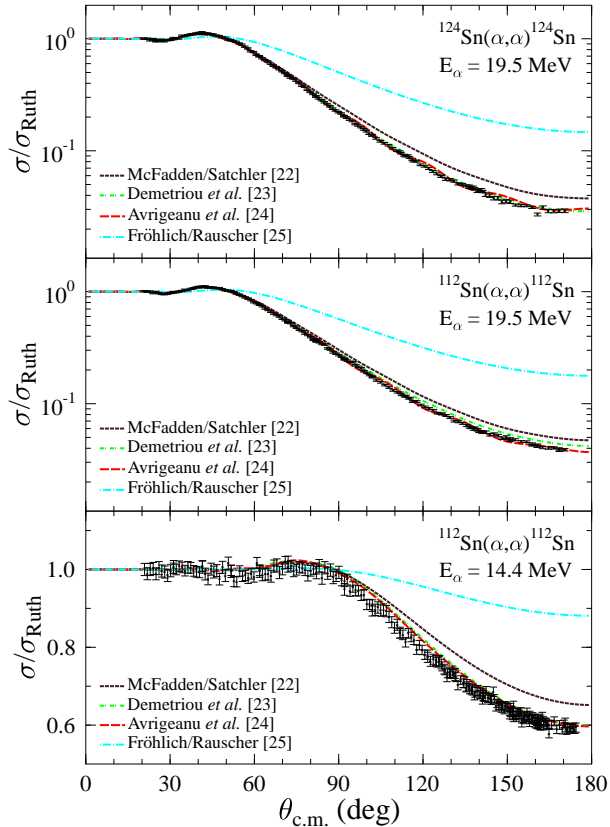


FIG. 3: (Color online) Ratio of the measured scattering cross sections of  $^{112}\text{Sn}(\alpha,\alpha)^{112}\text{Sn}$  at 14.4 MeV (lower diagram) and 19.5 MeV (middle) and  $^{124}\text{Sn}(\alpha,\alpha)^{124}\text{Sn}$  at 19.5 MeV (upper) to the Rutherford cross section. The predictions from the global  $\alpha$ -nucleus potentials from [22] (short dashed line), potential I from [23] (short dash-dotted line), [24] (long dashed line) and [25] (long dash-dotted line) are also shown. The overlap of the lines, mainly at forward angles, complicates their distinction. Note the logarithmic scale for the upper and middle diagrams ( $E_\alpha = 19.5$  MeV) and the linear scale for the lower diagram ( $E_\alpha = 14.4$  MeV).

### III. OPTICAL MODEL ANALYSIS

#### A. Angular distributions: comparison to theory

The theoretical analysis of the angular distributions is performed within the OM framework. The elastic scattering cross section can be calculated from the Schrödinger equation with the complex nuclear potential  $U(r)$  given by

$$U(r) = V_C(r) + V(r) + iW(r) \quad (3.1)$$

with the Coulomb potential  $V_C(r)$ , the real part  $V(r)$ , and the imaginary part  $W(r)$  of the nuclear potential.

The calculated differential cross sections for four different global  $\alpha$ -nucleus potentials are also presented in Fig. 3. The four-parameter Woods-Saxon potential from McFadden and Satchler [22] provides a rough description of the experimental data, overestimating the cross section in all three cases for backward angles. Potential I from Demetriou *et al.* [23] presents a good reproduction of the measured angular distributions, with a slight overestimation of the scattering cross sections at backward angles for the reaction  $^{112}\text{Sn}(\alpha,\alpha)^{112}\text{Sn}$  at  $E_\alpha = 19.5$  MeV. This potential, based on a double folding parameterization in its real part and a volume Woods-Saxon potential in its imaginary part, provides a good description of previous  $(\alpha,\alpha)$ ,  $(\alpha,n)$  and  $(\alpha,\gamma)$  cross section data.

The potential of Avrigeanu *et al.* [24], resulting from the investigation of  $\alpha$  scattering data at energies around the Coulomb barrier for  $A \approx 100$  nuclei, is also compared to the measured angular distributions. The potential is consistent with the experimental data, although the corresponding cross section presents a diffraction pattern at backward angles which is not observed in the measured data. Finally, the potential presented by Fröhlich and Rauscher [25], overestimates the cross section in all cases. This potential is an expansion of the McFadden and Satchler's potential to include  $(\alpha,n)$  and  $(\alpha,\gamma)$  cross section data at energies close to the astrophysically relevant region.

The depiction of the scattering cross section given by the different global potentials (Fig. 3) makes very difficult to state which potential provides the correct description of the experimental data. A global  $\alpha$ -nucleus potential must be able to describe the scattering cross section data along an isotopic chain, in order to demonstrate its reliability when extrapolating to unstable nuclei of interest for astrophysical applications. Despite the

striking qualitative similarities, the elastic scattering cross sections of  $^{112}\text{Sn}$  and  $^{124}\text{Sn}$  at  $E_\alpha = 19.5\text{ MeV}$  differ by roughly 30% at very backward angles. In Fig. 4, which shows the ratio of the two cross sections (divided by the Rutherford cross section) as a function of angle, all global  $\alpha$ -nucleus potentials of [22, 23, 24, 25] fail to reproduce either the strength or the oscillation pattern for backward angles. Thus, the use of these potentials in the extrapolation to more proton-rich species (of interest in  $p$  process nucleosynthesis) should be questioned.

The following section studies the angular distributions, extracting a local optical potential from the experimental data available.

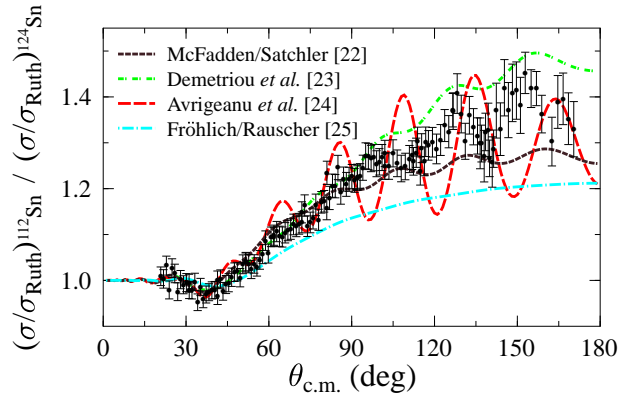


FIG. 4: (Color online) Ratio of the scattering cross sections  $(\sigma/\sigma_{\text{Ruth}})_{^{112}\text{Sn}}/(\sigma/\sigma_{\text{Ruth}})_{^{124}\text{Sn}}$  at  $E_\alpha = 19.5\text{ MeV}$  versus the angle in the center-of-mass frame. The predictions of the considered global  $\alpha$ -nucleus potentials are also shown. Minor differences for the c.m. angle (below  $0.2^\circ$ ) in the transformation to c.m. angles due to the different masses of  $^{112}\text{Sn}$  and  $^{124}\text{Sn}$  are neglected.

## B. Angular distributions: present experiment

In the present analysis, the real part of the potential is derived from a double-folding procedure with two adjustable parameters:

$$V(r) = \lambda \cdot V_{\text{F}}(r/w) \quad (3.2)$$

where  $V_{\text{F}}(r)$  is the double-folding potential which is calculated according to [26, 27, 28, 29] using the computer code DFOLD. The required density distributions of the  $\alpha$  particle and



the  $^{112,124}\text{Sn}$  nuclei were derived from measured charge density distributions [30]. We vary the strength of the double-folding potential by the parameter  $\lambda$ , adopting values around 1.2 and 1.4 (similar to previous works [18, 20, 29]). This reduces the so-called *family problem* of  $\alpha$ -nucleus potentials at low energies (see Refs. [18, 20] for detailed discussion). The width of the potential is adjusted using the parameter width  $w$ . We find values close to 1 for our data.

The different optical potentials can be compared through their total strengths or volume integrals, normalized to the number of interacting nucleon pairs ( $A_{\text{P}}A_{\text{T}}$ ), defined for both real and imaginary parts of the nuclear potential:

$$J_{\text{R}} = \frac{1}{A_{\text{P}}A_{\text{T}}} \int V(r) d^3r \quad (3.3)$$

$$J_{\text{I}} = \frac{1}{A_{\text{P}}A_{\text{T}}} \int W(r) d^3r \quad (3.4)$$

Both volume integrals are negative. In this work, we will only consider their absolute values.

The strength parameter  $\lambda$  has been adopted to take the linear form

$$\lambda = \frac{a^* + b^* \cdot E_{\text{c.m.}}}{J_{\text{R},0}} \quad (3.5)$$

where  $J_0$  is the volume integral of the double folding potential  $V_{\text{F}}(r/w)$ . The values for the parameters  $a^*$ ,  $b^*$  and  $J_{\text{R},0}$ , as extracted from the scattering data, are listed in Table I. The linear energy dependence adopted for  $^{112}\text{Sn}$  has been applied also for  $^{124}\text{Sn}$ , although we have measurements for only one energy for this nucleus. We check the validity of this linear dependence in Sect. III C, by analyzing the scattering data at higher energies. The parameter  $w$  allows a fine-tuning of the potential width; it remains very close to unity. A significant deviation of  $w$  from unity for stable nuclei, where the neutron and proton densities are very similar, would indicate that the nucleon-nucleon interaction is not well chosen. However, for nuclei with extremely high neutron-to-proton ratio one may expect the formation of neutron skins; in this case, such a deviation of  $w$  from unity should be found for nucleon density distributions derived from the proton density only.

The volume integral  $J_{\text{R}}$  for the real part of the nuclear potential adopted for the tin isotopes are shown in Figure 5, together with the values derived from the analysis of elastic scattering data on several doubly-magic and semi-magic nuclei in the energy range up to 140 MeV [18, 20, 29]. The data show a systematic smooth linear decrease at higher energies, in good agreement with the parameterization adopted for the  $^{112}\text{Sn}$  and  $^{124}\text{Sn}$  isotopes (solid

TABLE I: Optical potential parameters for the real ( $a^*$ ,  $b^*$ ,  $J_{R,0}$ ,  $w$ ) and imaginary parts of the nuclear potential. The parameters of the volume (V) and surface (S) Woods-Saxon potentials ( $W$ ,  $R$ ,  $a$ ) used in the imaginary part of the nuclear potential are shown together with the volume integral  $J_I$ .

Isotope	$a^*$ (MeV·fm <sup>3</sup> )	$b^*$ (fm <sup>3</sup> )	$J_{R,0}$ (MeV·fm <sup>3</sup> )	$w$	$W_V$ (MeV)	$R_V$ (fm)	$a_V$ (fm)	$W_S$ (MeV)	$R_S$ (fm)	$a_S$ (fm)	$J_I$ (MeV·fm <sup>3</sup> )
<sup>112</sup> Sn	352.92	-0.652	277.85	1.004	-3.137	1.737	0.341	356.36	1.252	0.218	97.16
<sup>124</sup> Sn	355.12	-0.652	274.90	1.006	-2.467	1.723	0.296	212.22	1.230	0.299	74.29

line). The Gaussian parameterization, first suggested by [31] and modified in [20, 23], is shown as a dotted line up to 50 MeV, which they proposed for astrophysical energies.

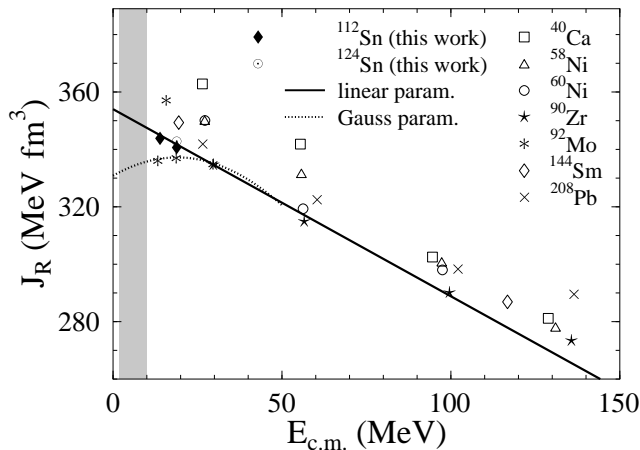


FIG. 5: Volume integral values  $J_R$  from the analysis of the measured data, together with values obtained in the study of elastic scattering data on doubly-magic and semi-magic nuclei [18, 20, 29]. The solid line shows a linear parameterization of  $J_R$  extracted from the data. The Gauss parameterization proposed by [23] for the description of low energy data (dotted line) is also shown below 50 MeV. The astrophysically relevant energy region for  $p$  process nucleosynthesis is shown by the grey area.

The imaginary part of the nuclear potential has been chosen as a sum of volume and surface Woods-Saxon potentials. The potential parameters (potential depth  $W_i$ , radius  $r_i = R_i \cdot A^{1/3}$  and diffuseness  $a_i$ , with  $i=V,S$ ) are listed in Table I. The relative weight

between the volume and the surface terms of the imaginary part of the nuclear potential is  $J_{I,V} = 0.22 \cdot J_{I,S}$ , as found in a study of the elastic scattering data in the  $A \approx 100$  mass region [32]. This dominance of the surface Woods-Saxon term at energies close to the Coulomb barrier provides a better description of  $\alpha$  capture data at the astrophysically interesting energy window [33].

The results of the OM analysis are compared in Fig. 6 to the experimental data from the three measured angular distributions. An excellent agreement is observed. An average value of  $\chi_{red}^2 = 1.1$  results from the analysis. Unlike other potentials, the ratio of the cross sections for the tin isotopes is reproduced with higher accuracy, as shown in Fig. 7.

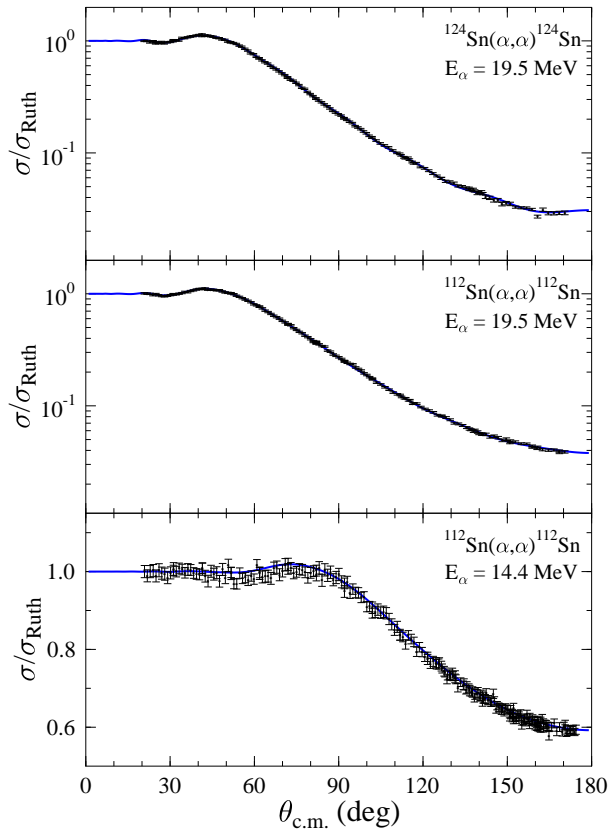


FIG. 6: Ratio of the measured scattering cross sections to the Rutherford cross section (same as in Fig. 3) including the results of the OM analysis performed for both tin nuclei (solid line).

In order to test the reliability of the obtained optical potentials, and observe its possible energy dependence, the following section compares the results of the OM analysis to other elastic scattering data measured at higher energies.

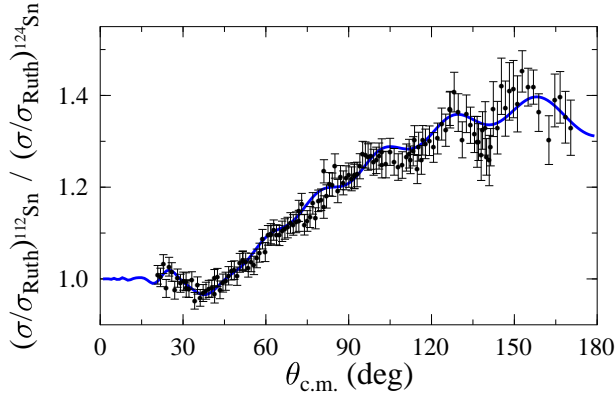


FIG. 7: Ratio of the scattering cross sections  $(\sigma/\sigma_{\text{Ruth}})_{^{112}\text{Sn}}/(\sigma/\sigma_{\text{Ruth}})_{^{124}\text{Sn}}$  at  $E_\alpha = 19.5$  MeV versus the angle in the center-of-mass frame including the results of the OM analysis performed in both tin nuclei (solid line). A significant improvement of the description of the experimental data is achieved.

### C. Angular distributions: comparison to other experiments

The angular distribution of elastically scattered  $\alpha$  particles on the tin isotopes  $^{112}\text{Sn}$  [34] and  $^{124}\text{Sn}$  [35] has been measured at energies far above the Coulomb barrier. These data are shown in Fig. 8 for the reactions  $^{112}\text{Sn}(\alpha,\alpha)^{112}\text{Sn}$  at  $E_\alpha \approx 50$  MeV (left part of the Figure) and  $^{124}\text{Sn}(\alpha,\alpha)^{124}\text{Sn}$  at  $E_\alpha \approx 25$  MeV (right part of the Figure). In addition, the predictions from the optical potentials derived from the analysis of our elastic scattering data are shown.

The reproduction of the data from the reaction  $^{124}\text{Sn}(\alpha,\alpha)^{124}\text{Sn}$  [35] is satisfactory. The diffraction pattern shown by the experimental data from the reaction  $^{112}\text{Sn}(\alpha,\alpha)^{112}\text{Sn}$  [34], measured at energies far above from the Coulomb barrier, is not described well. However, a minor variation of the potential parameters (solid line) in which the contribution of the volume term to the imaginary part of the nuclear potential is increased ( $J_{I,V} = 0.79 J_{I,S}$ ) provides an improved description of the scattering data from [34]. In the case of the scattering data from [35], closer to the energy region measured in this work, a renormalization of the scattering data with a factor of 1.2 would provide a better agreement between the experimental data and the calculated cross section.

From this analysis, the imaginary part of the nuclear potential shows a stronger energy dependence at energies higher than those considered in this work. Without more experimental data for the nuclei studied, it is not possible to predict the possible energy dependence

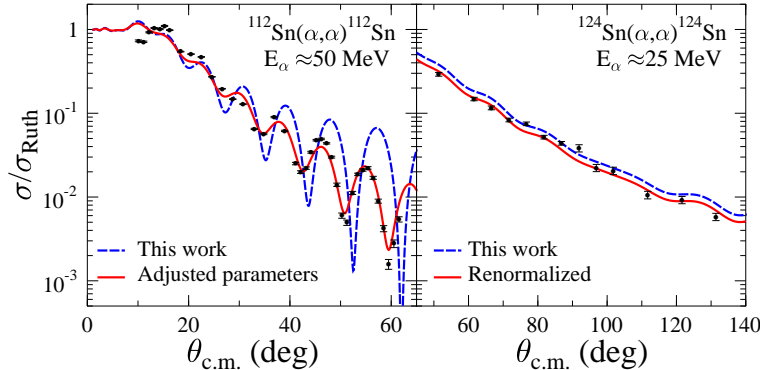


FIG. 8: (Color online) Elastic scattering data from the reactions  $^{112}\text{Sn}(\alpha,\alpha)^{112}\text{Sn}$  at  $E_\alpha \approx 50$  MeV [34] (left part of the Figure) and  $^{124}\text{Sn}(\alpha,\alpha)^{124}\text{Sn}$  at  $E_\alpha \approx 25$  MeV [35] (right part of the Figure). The predictions from the derived potentials from the elastic scattering data presented in this work are also shown (dashed line). Results from a readjustment of the potential parameters (left) and a normalization of the cross section (right) are shown as a solid line. For details see text.

of both terms in the imaginary part of the nuclear potential.

#### D. Excitation function: comparison to other experiments

The excitation function of the elastically scattered  $\alpha$  particles on the nucleus  $^{112}\text{Sn}$  at very backward angles ( $\vartheta_{\text{c.m.}} = 178^\circ$ ) was measured by Badawy *et al.* [36] at different energies below and above the Coulomb barrier. The experimental data are shown in Fig. 9. The successful reproduction of the experimental data confirms the good knowledge of the  $\alpha$ -nucleus potential (solid line) in the considered energy region.

## IV. THE $^{112}\text{Sn}(\alpha,\gamma)^{116}\text{Te}$ REACTION

A relevant test of the potentials for astrophysical purposes consists of the reproduction of the  $(\alpha,\gamma)$  reaction cross sections at energies close to the Gamow window. In this section, the main features of the statistical model are presented, followed by a comparison of existing experimental data from the reaction  $^{112}\text{Sn}(\alpha,\gamma)^{116}\text{Te}$  to the predictions from the different  $\alpha$ -nucleus potentials.

The main ingredients of the statistical model (Hauser-Feshbach approach) [9] in the calcu-

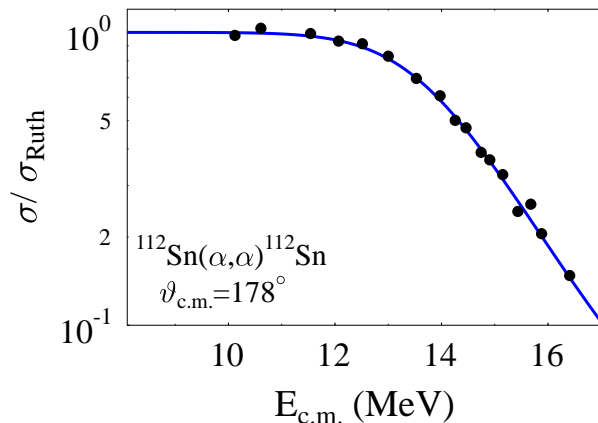


FIG. 9: Excitation function of the nucleus  $^{112}\text{Sn}$  at  $\vartheta_{\text{c.m.}} = 178^\circ$  [36]. The results from the derived  $\alpha$ -nucleus potential are also shown (solid line). The nice reproduction of the experimental data confirms the good knowledge of the  $\alpha$ -nucleus potential in this energy region.

lation of reaction rates under astrophysical conditions are transmission coefficients (particle and radiative), nuclear level densities and optical potentials [37]. These elements allow the calculation of the reaction cross section in astrophysical scenarios. Once  $\sigma^*(E)$  is calculated, considering the case of the  $\alpha$  capture reaction, the reaction rate per particle pair at a given stellar temperature  $T^*$  is defined by [37]:

$$\langle\sigma v\rangle^* = \left(\frac{8}{\pi\mu}\right)^{1/2} \frac{1}{(kT^*)^{3/2}} \int_0^\infty \sigma_{(\alpha,\gamma)}^*(E) E \exp\left(-\frac{E}{kT^*}\right) dE \quad (4.1)$$

by folding the stellar reaction cross section  $\sigma_{(\alpha,\gamma)}^*(E)$  with the Maxwell-Boltzmann velocity distribution of the incident particles.  $\mu$  is the reduced mass of the system. In a stellar plasma, nuclei are in thermal equilibrium with the environment and therefore can be found also in excited states. The stellar reaction cross section  $\sigma^* = \sum_{\lambda\nu} \sigma^{\lambda\nu}$  includes transitions from all populated target states  $\lambda$  to all energetically reachable final states  $\nu$  whereas a laboratory cross section  $\sigma^{\text{lab}} = \sum_{\nu} \sigma^{0\nu}$  only accounts for transitions from the ground state of the target. However, for the case of  $^{112}\text{Sn}(\alpha,\gamma)$  the stellar enhancement  $\sigma^*/\sigma^{\text{lab}}$  is negligible in the  $p$  process temperature range because no low-lying excited states in  $^{112}\text{Sn}$  are available for population. The product in the integrand of Eq. 4.1 leads to a maximum, defining an effective energy window (the so-called *Gamow window*) where most of the reactions occur. The reaction cross section should be determined in this energy region. The photo-

disintegration rate is then derived from the capture rate applying detailed balance (see e.g. [37]).

During  $p$  process nucleosynthesis, typical temperatures of  $2.0 \leq T_9 \leq 3.0$  are reached (where  $T_9$  is the temperature in GK). This corresponds to an energy window between 5.1 and 9.6 MeV for the  $\alpha$  capture reaction, or between 4.2 and 8.7 MeV for the photon-induced ( $\gamma, \alpha$ ) reaction ( $Q_\alpha(^{116}\text{Te}) = 930$  keV) [38].

Due to the astrophysical interest, the laboratory ( $\alpha, \gamma$ ) reaction cross section on the nucleus  $^{112}\text{Sn}$  has been measured [16] at energies close to the Gamow window. The astrophysical S-factor of the reaction  $^{112}\text{Sn}(\alpha, \gamma)^{116}\text{Te}$  is shown in Fig. 10. In addition, the predictions from the global  $\alpha$ -nucleus potentials and the optical potential derived in this work are also plotted. Because of the scarce experimental data available on the  $^{112}\text{Sn}(\alpha, \gamma)^{116}\text{Te}$  reaction, we can only perform a very limited comparison.

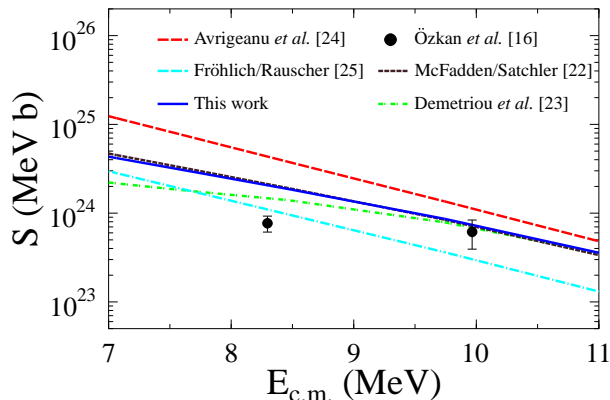


FIG. 10: (Color online) Astrophysical S-factor of the  $^{112}\text{Sn}(\alpha, \gamma)^{116}\text{Te}$  capture reaction. The experimental data from [16] are compared to the predictions from the global  $\alpha$ -nucleus potentials and the optical potential obtained from the analysis of the elastic scattering data. The potential from [25] presents the best reproduction of the experimental data. The prediction from the optical potential derived in this work presents a satisfactory description of the measured cross sections, similar to the potential from [22].

The global parameterization from [25] provides a satisfactory description of the few experimental data, in contrast to its poor agreement with the elastic scattering data. The other potentials, with the exception of [24], reproduce the cross section data well. The potential obtained from the analysis of the elastic scattering data presented in this work (Sec. III B)

provides a satisfactory description of the  $(\alpha,\gamma)$  data, very similar to that of [22]. However, further  $\alpha$  capture experiments on the nucleus  $^{112}\text{Sn}$  should be performed in order to cover the whole *Gamow window*. Experiments are under way [39]. These data should help to determine the experimental energy dependence of the astrophysical S-factor.

As mentioned, once the astrophysical  $(\alpha,\gamma)$  capture cross section has been calculated, it is possible to derive the corresponding astrophysical capture and photo-disintegration rates [12, 37]. For a comparison of the results provided by the different parameterizations of [22, 23, 24, 25], the variation of the obtained reaction rates is shown in Table II, where the ratios of rates with respect to the rate obtained using [25] are presented. All other ingredients of the statistical model calculations have been kept fixed as in [37].

The different potentials predict reaction rates which deviate up to a factor of 8. In the typical temperature window for the  $p$  process, the reaction rates obtained by using the optical potential derived from the elastic scattering predict in average a rate which is around 50% higher than that of [25], remaining very close to the values from McFadden and Satchler [22].

## V. SUMMARY

We have measured the elastic scattering cross section of  $^{112,124}\text{Sn}(\alpha,\alpha)^{112,124}\text{Sn}$  at energies  $E_\alpha = 19.5$  MeV and 14.4 MeV. The data have been compared to various global  $\alpha$ -nucleus potentials. The potentials from [23] and [24] provide a satisfactory description of the elastic scattering data, in contrast to the potentials from [22] and [25], which deviate considerably from the measured angular distributions. None of the global potentials is able to reproduce the ratio between the cross sections on the proton- and neutron-rich tin isotopes. Consequently, any extrapolation to  $\alpha$ -nucleus potentials for unstable neutron-deficient nuclei on the  $p$  process path remains uncertain.

The present analysis performed within the OM framework provided a remarkable reproduction of the measured angular distributions. It has been used in the analysis of literature data at different energies [34, 35, 36]. The results fit well with the systematic behavior of  $\alpha$ -nucleus folding potentials.

Most of the global  $\alpha$ -nucleus potentials (with the exception of [24]), as well as the potential obtained from the OM analysis, describe the few existing  $^{112}\text{Sn}(\alpha,\gamma)^{116}\text{Te}$  cross section data points well; however, the energy dependence of the astrophysical S-factor is not well de-



TABLE II: Ratio between the reaction rates obtained from the different  $\alpha$ -nucleus potentials compared to the reaction rate of [25],  $\langle\sigma v\rangle_{[i]}^*/\langle\sigma v\rangle_{[25]}^*$ , as a function of the temperature  $T_9$ . The typical temperature range for  $p$  process nucleosynthesis ( $2.0 \leq T_9 \leq 3.0$ ) is shown.

$T_9$	$\langle\sigma v\rangle_{[i]}^*/\langle\sigma v\rangle_{[25]}^*$			
	[22]	[23]	[24]	This work
0.2	0.784	0.126	4.760	0.672
0.4	0.794	0.130	4.719	0.681
0.6	0.844	0.167	4.726	0.722
0.8	0.915	0.311	4.664	0.786
1.0	0.993	0.483	4.610	0.855
1.5	1.187	0.542	4.479	1.044
2.0	1.397	0.621	4.327	1.262
2.5	1.605	0.846	4.169	1.495
3.0	1.795	1.142	4.035	1.714
3.5	1.961	1.453	3.941	1.927
4.0	2.106	1.735	3.868	2.106
5.0	2.343	2.217	3.809	2.422
6.0	2.500	2.515	3.804	2.638
8.0	2.664	2.808	3.821	2.856
10.0	2.752	2.962	3.800	2.981

terminated from the theoretical predictions. The resulting stellar rates for the  $^{112}\text{Sn}(\alpha,\gamma)^{116}\text{Te}$  as well as  $^{116}\text{Te}(\gamma,\alpha)^{112}\text{Sn}$  reactions deviate in the energy region considered for  $p$  process calculations by up to a factor of 8.

The present data provide an excellent tool to test the behaviour of global  $\alpha$ -nucleus potentials. Additional elastic scattering experiments are needed in the  $p$  process mass range at energies around the Coulomb barrier.

## Acknowledgments

We would like to thank the cyclotron team of ATOMKI for the excellent beam during the experiment. Two of us (D. G., P. M.) gratefully acknowledge the kind hospitality at ATOMKI. We thank N. T. Burtebayev and O. Bespalova for providing the numerical data for Refs. [34] and [35], respectively. We also thank M. Howard for reading the manuscript carefully. This work was supported by DFG (SFB634 and FOR 272/2-2) and OTKA (T034259, T042733, F043408, D048283). T. R. is supported by the Swiss NSF (grants 2024-067428.01, 2000-061031.02, 2000-105328). Zs. F. and Gy. Gy. acknowledge support from a Bolyai grant.

- 
- [1] E. Burbidge, G. Burbidge, W. Fowler, and F. Hoyle, *Rev. Mod. Phys.* **29**, 547 (1957).
  - [2] S. E. Woosley and W. M. Howard, *Astrophys. J. Suppl.* **36**, 285 (1978).
  - [3] K. Langanke and M. Wiescher, *Rep. Prog. Phys.* **64**, 1657 (2001).
  - [4] T. Rauscher, A. Heger, R. D. Hoffman, and S. E. Woosley, *Astrophys. J.* **576**, 323 (2002).
  - [5] M. Arnould and S. Goriely, *Phys. Rep.* **384**, 1 (2003).
  - [6] V. Costa, M. Rayet, R. A. Zappalà, and M. Arnould, *Astron. Astroph.* **358**, 67 (2000).
  - [7] W. Rapp, Report FZKA 6956, Forschungszentrum Karlsruhe (2004).
  - [8] T. Rauscher, *Nucl. Phys. A* (2005), in press.
  - [9] W. Hauser and H. Feshbach, *Phys. Rev.* **87**, 366 (1952).
  - [10] T. Rauscher and F.-K. Thielemann, in *Stellar Evolution, Stellar Explosions and Galactic Chemical Evolution. Proceedings of the Second Oak Ridge Symposium on Atomic and Nuclear Astrophysics, 1997*, edited by A. Mezzacappa (IOP, Bristol, 1998), p. 519.
  - [11] S. Goriely, in *10<sup>th</sup> Int. Symp. Capture Gamma-Ray Spectroscopy*, edited by S. Wender (AIP Conference Proceedings **529**, 2000), p. 287.
  - [12] T. Rauscher and F.-K. Thielemann, *At. Data Nucl. Data Tables* **79**, 47 (2001).
  - [13] T. Rauscher and F.-K. Thielemann, *At. Data Nucl. Data Tables* **88**, 1 (2004).
  - [14] Z. Fülöp, A. Z. Kiss, E. Somorjai, C. E. Rolfs, H. P. Trautvetter, T. Rauscher, and H. Oberhummer, *Z. Phys. A* **355**, 203 (1996).
  - [15] W. Rapp, M. Heil, D. Hentschel, F. Käppeler, R. Reifarth, H. J. Brede, H. Klein, and T. Rauscher, *Phys. Rev. C* **66**, 015803 (2002).

- [16] N. Özkan, A. S. J. Murphy, R. N. Boyd, A. L. Cole, M. Famiano, R. T. Güray, M. Howard, L. Şahin, J. J. Zach, R. deHaan, et al., Nucl. Phys. **A710**, 469 (2002).
- [17] E. Somorjai, Z. Fülöp, A. Z. Kiss, C. E. Rolfs, H. P. Trautvetter, U. Greife, M. Junker, S. Goriely, M. Arnould, M. Rayet, et al., Astron. Astroph. **333**, 1112 (1998).
- [18] P. Mohr, T. Rauscher, H. Oberhummer, Z. Máté, Z. Fülöp, E. Somorjai, M. Jaeger, and G. Staudt, Phys. Rev. C **55**, 1523 (1997).
- [19] T. Rauscher, F.-K. Thielemann, and H. Oberhummer, Astrophys. J. **451**, L37 (1995).
- [20] Z. Fülöp, G. Gyürky, Z. Máté, E. Somorjai, L. Zolnai, D. Galaviz, M. Babilon, P. Mohr, A. Zilges, T. Rauscher, et al., Phys. Rev. C **64**, 065805 (2001).
- [21] Z. Máté, S. Szilágyi, L. Zolnai, A. Bredbacka, M. Brenner, K.-M. Källmann, and P. Manngård, Acta Phys. Hung. **65**, 287 (1989).
- [22] L. McFadden and G. R. Satchler, Nucl. Phys. **84**, 177 (1966).
- [23] P. Demetriou, C. Grama, and S. Goriely, Nucl. Phys. **A707**, 253 (2002).
- [24] M. Avrigeanu, W. von Oertzen, A. J. M. Plompen, and V. Avrigeanu, Nucl. Phys. **A723**, 104 (2003).
- [25] T. Rauscher, Nucl. Phys. **A719**, 73c; Erratum: Nucl. Phys. **A725** (2003) 295 (2003).
- [26] A. M. Kobos, B. A. Brown, R. Lindsay, and G. R. Satchler, Nucl. Phys. **A425**, 205 (1984).
- [27] G. R. Satchler and W. G. Love, Phys. Rep. **55**, 183 (1979).
- [28] H. Abele and G. Staudt, Phys. Rev. C **47**, 742 (1993).
- [29] U. Atzrott, P. Mohr, H. Abele, C. Hillenmayer, and G. Staudt, Phys. Rev. C **53**, 1336 (1996).
- [30] H. de Vries, C. W. de Jager, and C. de Vries, At. Data Nucl. Data Tables **36**, 495 (1987).
- [31] P. Mohr, Phys. Rev. C **61**, 045802 (2000).
- [32] D. Galaviz, Ph.D. thesis, Technische Universität Darmstadt (2004).
- [33] T. Rauscher, in *Proc. IX Workshop on Nuclear Astrophysics*, edited by W. Hillebrandt and E. Müller (MPA, Garching, 1998), pp. 84; nucl-th/0007070.
- [34] N. T. Burtebaev, K. A. Kuterbekov, and I. N. Kukhtina, Sov. J. Nucl. Phys. **51**, 827 (1990).
- [35] O. V. Bespalova, E. A. Romanovskij, N. G. Gorjaga, N. M. Kha, B. S. Galakhmatova, L. M. Rafu, S. I. Fedoseev, D. Lam, and A. Belal, Yad. Fiz. **56**, 113 (1992).
- [36] I. Badawy, B. Berthier, P. Charles, M. Dost, B. Fernandez, J. Gastebois, and S. M. Lee, Phys. Rev. C **17**, 978 (1978).
- [37] T. Rauscher and F.-K. Thielemann, At. Data Nucl. Data Tables **75**, 1 (2000).

- [38] P. Mohr, M. Babilon, D. Galaviz, K. Sonnabend, K. Vogt, and A. Zilges, Nucl. Phys. **A719**, 90c (2003).
- [39] W. Rapp, private communication (2004).